

Computing Residual Diffusivity by Adaptive Basis Learning via Spectral Method

Jiancheng Lyu, Jack Xin* and Yifeng Yu

Department of Mathematics, University of California at Irvine, Irvine, CA 92697, USA

Received 9 November 2016; Accepted (in revised version) 26 January 2017

Dedicated to Professor Zhenhuan Teng on the occasion of his 80th birthday

Abstract. We study the residual diffusion phenomenon in chaotic advection computationally via adaptive orthogonal basis. The chaotic advection is generated by a class of time periodic cellular flows arising in modeling transition to turbulence in Rayleigh-Bénard experiments. The residual diffusion refers to the non-zero effective (homogenized) diffusion in the limit of zero molecular diffusion as a result of chaotic mixing of the streamlines. In this limit, the solutions of the advection-diffusion equation develop sharp gradients, and demand a large number of Fourier modes to resolve, rendering computation expensive. We construct adaptive orthogonal basis (training) with built-in sharp gradient structures from fully resolved spectral solutions at few sampled molecular diffusivities. This is done by taking snapshots of solutions in time, and performing singular value decomposition of the matrix consisting of these snapshots as column vectors. The singular values decay rapidly and allow us to extract a small percentage of left singular vectors corresponding to the top singular values as adaptive basis vectors. The trained orthogonal adaptive basis makes possible low cost computation of the effective diffusivities at smaller molecular diffusivities (testing). The testing errors decrease as the training occurs at smaller molecular diffusivities. We make use of the Poincaré map of the advection-diffusion equation to bypass long time simulation and gain accuracy in computing effective diffusivity and learning adaptive basis. We observe a non-monotone relationship between residual diffusivity and the amount of chaos in the advection, though the overall trend is that sufficient chaos leads to higher residual diffusivity.

AMS subject classifications: 76R99, 35B27, 65T40, 65M70

Key words: Advection-diffusion, chaotic flows, effective diffusion, adaptive basis learning, residual diffusion.

*Corresponding author. *Email addresses:* jianchel@uci.edu (J. C. Lyu), jxin@math.uci.edu (J. Xin), yyu1@math.uci.edu (Y. F. Yu)

1. Introduction

Diffusion enhancement in fluid advection has been studied for nearly a century, dating back to the pioneering work of Taylor [13] in 1921. It is a fundamental problem to characterize and quantify the large scale effective diffusion (denoted by D^E) in fluid flows containing complex and turbulent streamlines. Much progress has been made based on the passive scalar model [9]:

$$T_t + (\mathbf{v} \cdot \nabla) T = D_0 \Delta T, \quad (1.1)$$

where T is a scalar function (e.g., temperature or concentration), $D_0 > 0$ is a constant (the so called molecular diffusion), $\mathbf{v}(\mathbf{x}, t)$ is a prescribed incompressible velocity field, ∇ and Δ are the spatial gradient and Laplacian operators.

When the flow is steady, periodic and two dimensional, precise asymptotics of D^E are known. A prototypical example is the steady cellular flow [4, 5], $\mathbf{v} = (-H_y, H_x)$, $H = \sin x \sin y$, see also [11, 14, 15] for its application in effective speeds of front propagation. The asymptotics of the effective diffusion along any unit direction in the cellular flow obeys the square root law in the advection dominated regime: $D^E = O(\sqrt{D_0}) \gg D_0$ as $D_0 \downarrow 0$, [5, 6]. This is intuitively due to the ordered streamlines of the steady cellular flows where enhanced transport occurs along saddle to saddle connections and a diffusing particle escapes closed streamlines by hopping from cell to cell. However, if the streamlines are fully chaotic (well-mixed), the enhancement can follow a very different law. The simplest such example is the time periodic cellular flow:

$$\mathbf{v} = (\cos(y), \cos(x)) + \theta \cos(t)(\sin(y), \sin(x)), \quad \theta \in (0, 1]. \quad (1.2)$$

The first term of (1.2) is a steady cellular flow with a $\pi/4$ rotation, and the second term is a time periodic perturbation that introduces an increasing amount of disorder in the flow trajectories as θ becomes larger. At $\theta = 1$, it is fully mixing, and empirically sub-diffusive [17]. The flow (1.2) has served as a model of chaotic advection for Rayleigh-Bénard experiment [3]. Numerical simulations [2, 10] suggest that at $\theta = 1$, the effective diffusion along the x -axis, $D_{11}^E = O(1)$ as $D_0 \downarrow 0$, the so called *residual diffusion* arises. As $D_0 \downarrow 0$, the solutions develop sharp gradients, and render accurate computation costly, especially if one is interested in D^E parametrized by θ .

Let us recall the formula for effective diffusivity tensor [2]:

$$D_{ij}^E = D_0 (\delta_{ij} + \langle Dw_i \cdot Dw_j \rangle), \quad (1.3)$$

where w is a mean zero space-time periodic vector solution of:

$$w_t + (\mathbf{v} \cdot \nabla) w - D_0 \Delta w = -\mathbf{v}, \quad (1.4)$$

and the bracket denotes space-time average over the periods. The solution of (1.4) is unique by the Fredholm alternative. The correction to D_0 is positive definite in (1.3).

In this paper, we shall construct adaptive basis functions to handle the singular solutions of (1.4) at small D_0 . First, we compute w by the spectral method, because

Fourier basis can represent cellular flow with few modes. By truncating the Fourier expansion, we find an approximate system of ordinary differential equations (ODEs). The time periodic solution is constructed as the unique fixed point of the Poincaré map of the ODE's time 2π flow. The snapshots of solutions in the time interval $[0, 2\pi]$ are saved into columns of a matrix W . The adaptive basis functions are left singular eigenvectors corresponding to the top singular values of W . This is the training process for adaptive basis, and is done at a few sampled D_0 or θ values. The Eq. (1.4) at other D_0 or $\theta \in (0, 1]$ will be solved in terms of the adaptive basis trained at the closest sample D_0 or θ value. Then formula (1.3) is used to calculate D^E . We shall see that the number of adaptive basis functions is under a few hundred, much less than that of Fourier basis by several orders of magnitude. The relative error of the adaptive solution from a resolved spectral solution is under 6.5 % when testing at $D_0 = 10^{-5}$ and training at $D_0 = 10^{-4}$. Thus we manage to achieve accurate enough solutions at much lower costs in the regime of small D_0 where the number of Fourier basis functions grows rapidly.

The procedure of taking snapshots and performing singular value decomposition (SVD) is standard in reduced order modeling [12] and is known as proper orthogonal decomposition (POD) in the fluid dynamics literature [7, 8]. The residual diffusivity problem we study here however offers an ideal testing ground for the evaluation of POD which lacks theoretical guarantees in general. The success of POD relies on the underlying dynamics being governed by a unique low dimensional attractor. In our case, the time periodicity of v helps to reduce the evolution problem (1.4) to a Poincaré map problem. The snapshots (training data) are directly drawn from the time periodic solution, hence more effective for learning. The testing of adaptive basis and the resulting error rates at the out-of-sample D_0 or θ values also provide quantitative measures for future development of adaptive basis.

The rest of the paper is organized as follows. In section 2, we derive (1.3)-(1.4), and project (1.4) onto Fourier basis functions to arrive at a finite system of ODEs upon truncation. We then formulate the periodic solution w as a fixed point of Poincaré map, show related numerical scheme and computational results on residual diffusion. A new finding is that the residual diffusion has a non-monotone dependence on θ . In section 3, we outline the adaptive basis training procedure and present testing results on a broad range of out-of-sample D_0 or θ values. The energy distribution across the adaptive basis functions is much more localized than that over the Fourier basis, indicating that the sharp gradient structures are captured in the adaptive basis functions. Concluding remarks are in section 4.

2. Residual diffusivity and Poincaré map

2.1. Effective diffusivity

Let $v(x, t)$ be a velocity flow periodic in $x \in \mathbf{R}^2$ and t , $\nabla \cdot v = 0$ and have mean zero. The advection-diffusion (passive scalar) equation is

$$u_t + (\mathbf{v} \cdot \nabla) u = D_0 \Delta u, \quad (2.1)$$

where $D_0 > 0$ is a constant.

Remark 2.1. Since $\mathbf{v}(\mathbf{x}, t)$ is incompressible and has mean zero in space, there exists a 2×2 skew-symmetric matrix $\mathbf{H} = (H_{ij}(\mathbf{x}, t))$ such that $\nabla \cdot \mathbf{H} = \mathbf{v}$. In fact, without loss of generality, suppose $\mathbf{v}(\mathbf{x}, t)$ is 2π -periodic in spatial and temporal variables, and $\mathbf{v} = (v_1, v_2)$. Define

$$H_{pq}(\mathbf{x}, t) = \frac{1}{i} \sum_{\mathbf{k} \neq \mathbf{0}} e^{i\mathbf{k} \cdot \mathbf{x}} \frac{k_p v_{q,\mathbf{k}}(t) - k_q v_{p,\mathbf{k}}(t)}{|\mathbf{k}|^2},$$

for $p, q = 1, 2$, where

$$v_p(\mathbf{x}, t) = \sum_{\mathbf{k} \in \mathbf{Z}^2} e^{i\mathbf{k} \cdot \mathbf{x}} v_{p,\mathbf{k}}(t), \quad p = 1, 2.$$

It follows from $\nabla \cdot \mathbf{v} = 0$ that $\nabla \cdot \mathbf{H} = \mathbf{v}$. Hence Eq. (2.1) can be written in the form

$$u_t - (a_{ij}(\mathbf{x}, t) u_{x_j})_{x_i} = 0,$$

where

$$a_{ij}(\mathbf{x}, t) = D_0 \delta_{ij} + H_{ij}(\mathbf{x}, t).$$

The matrix $(a_{ij}(\mathbf{x}, t))$ is periodic and uniformly elliptic for $D_0 > 0$.

In the large-distance and large-time scaling $\mathbf{x} \rightarrow \mathbf{x}/\epsilon$, $t \rightarrow t/\epsilon^2$, Eq. (2.1) becomes

$$u_t^\epsilon(\mathbf{x}, t) + \frac{1}{\epsilon} \left(\mathbf{v} \left(\frac{\mathbf{x}}{\epsilon}, \frac{t}{\epsilon^2} \right) \cdot \nabla \right) u^\epsilon(\mathbf{x}, t) = D_0 \Delta u^\epsilon(\mathbf{x}, t).$$

Initial data are independent of ϵ ,

$$u^\epsilon(\mathbf{x}, 0) = U(\mathbf{x}).$$

Solution can be sought as a multi-scale expansion of the form:

$$u^\epsilon(\mathbf{x}, t) = u^{(0)}(\mathbf{x}, t; \mathbf{y}, \tau) + \epsilon u^{(1)}(\mathbf{x}, t; \mathbf{y}, \tau) + \epsilon^2 u^{(2)}(\mathbf{x}, t; \mathbf{y}, \tau) + \cdots,$$

where $\mathbf{y} = \mathbf{x}/\epsilon$ and $\tau = t/\epsilon^2$.

Let ∂ and ∇ denote gradient operator with respect to fast and slow space variables respectively, $\mathbf{w}(\mathbf{x}, t)$ be the periodic solution with vanishing average over periodicities to the cell problem

$$\mathbf{w}_t(\mathbf{x}, t) + (\mathbf{v}(\mathbf{x}, t) \cdot \nabla) \mathbf{w}(\mathbf{x}, t) - D_0 \nabla^2 \mathbf{w}(\mathbf{x}, t) = -\mathbf{v}(\mathbf{x}, t). \quad (2.2)$$

It can be calculated directly that $u^{(0)}$ and $u^{(1)}$ are in the form

$$\begin{aligned} u^{(0)}(\mathbf{x}, t; \mathbf{y}, \tau) &= u^{(0)}(\mathbf{x}, t), \\ u^{(1)}(\mathbf{x}, t; \mathbf{y}, \tau) &= u^{(1)}(\mathbf{x}, t) + \mathbf{w}(\mathbf{y}, \tau) \cdot \nabla u^{(0)}(\mathbf{x}, t). \end{aligned}$$

Solvability of the equation

$$u_{\tau}^{(2)} + (\mathbf{v} \cdot \partial) u^{(2)} - D_0 \partial^2 u^{(2)} = -u_t^{(0)} - (\mathbf{v} \cdot \nabla) u^{(1)} + D_0 \nabla^2 u^{(0)} + 2D_0 \partial \cdot \nabla u^{(1)}$$

implies the zero average of the right-hand side, so $u^{(0)}$ satisfies the effective equation

$$\begin{aligned} u_t^{(0)}(\mathbf{x}, t) &= D_{ij}^E \nabla^2 u^{(0)}(\mathbf{x}, t), \\ u^{(0)}(\mathbf{x}, 0) &= U(\mathbf{x}), \end{aligned}$$

where the effective diffusivity tensor

$$D_{ij}^E = D_0 (\delta_{ij} + \langle \partial \mathbf{w}_i \cdot \partial \mathbf{w}_j \rangle),$$

and $\langle \cdot \rangle$ denotes space time average. Given $(a_{ij}(\mathbf{x}, t))$ defined in Remark 2.1 being periodic and uniformly elliptic, Theorem 2.1 in Chapter 2 of [1] says that u^ϵ converges to $u^{(0)}$ weakly in the L^2 sense as $\epsilon \downarrow 0$.

Explicit upper and lower bounds of D^E are known [6] when $\mathbf{v}(\mathbf{x}, t) = \nabla^\perp H(\mathbf{x})$ is time independent. Under appropriate assumptions on $H(\mathbf{x})$, in particular for steady cellular flows (Eq. (1.2) with $\theta = 0$),

$$D_{ii}^E = \mathcal{O}(\sqrt{D_0}), \quad i = 1, 2, \quad D_0 \downarrow 0.$$

For n -dimensional steady flow, $n \geq 2$, see [16] for the asymptotic limit of $D_0 D^E$ as D_0 tends to zero. Shear layer structure is the typical case when the limit is not zero. Numerical results [2, 10] suggest that if the streamlines of the flow are chaotic,

$$D_{11}^E = \mathcal{O}(1), \quad D_0 \downarrow 0.$$

We shall recover this result and compute also D_{12}^E with our method.

2.2. ODEs from Fourier basis

Let us write $\mathbf{v} = (v, \tilde{v})$ and $\mathbf{w} = (w, \tilde{w})$ in component form. Consider the first equation in the cell problem (2.2):

$$w_t + (\mathbf{v} \cdot \partial) w - D_0 \partial^2 w = -v. \tag{2.3}$$

Eq. (2.3) can be rewritten as an infinite system of ODEs of Fourier modes

$$\frac{dw_{\mathbf{k}}}{dt} + D_0 |\mathbf{k}|^2 w_{\mathbf{k}} + i \sum_{\mathbf{j} \in \mathbf{Z}^2} [(k_1 - j_1) v_{\mathbf{j}}(t) + (k_2 - j_2) \tilde{v}_{\mathbf{j}}(t)] w_{\mathbf{k}-\mathbf{j}} = -v_{\mathbf{k}}(t),$$

where

$$w = \sum_{\mathbf{k} \in \mathbf{Z}^2} w_{\mathbf{k}}(t) e^{i\mathbf{k} \cdot \mathbf{x}}, \quad v = \sum_{\mathbf{k} \in \mathbf{Z}^2} v_{\mathbf{k}}(t) e^{i\mathbf{k} \cdot \mathbf{x}}, \quad \tilde{v} = \sum_{\mathbf{k} \in \mathbf{Z}^2} \tilde{v}_{\mathbf{k}}(t) e^{i\mathbf{k} \cdot \mathbf{x}}.$$

Set $\|\mathbf{k}\| = \max\{|k_1|, |k_2|\}$. A truncated solution with $(2N + 1)^2$ modes

$$w^N(\mathbf{x}, t) = \sum_{\|\mathbf{k}\| \leq N} w_{\mathbf{k}}^N(t) e^{i\mathbf{k} \cdot \mathbf{x}} \tag{2.4}$$

solves

$$\begin{aligned} & \frac{dw_{\mathbf{k}}^N}{dt} + D_0 |\mathbf{k}|^2 w_{\mathbf{k}}^N + i \sum_{\|\mathbf{k}-\mathbf{j}\| \leq N} [(k_1 - j_1) v_{\mathbf{j}}(t) + (k_2 - j_2) \tilde{v}_{\mathbf{j}}(t)] w_{\mathbf{k}-\mathbf{j}}^N \\ & = -v_{\mathbf{k}}(t). \end{aligned} \tag{2.5}$$

Thus D_{11}^E is approximated by

$$D_{11, N}^E = D_0 \left(1 + \sum_{\|\mathbf{k}\| \leq N} |\mathbf{k}|^2 \langle w_{\mathbf{k}}^N \overline{w_{\mathbf{k}}^N} \rangle \right).$$

2.3. Poincaré map

Vectorize $\{w_{\mathbf{k}}^N(t)\}_{\|\mathbf{k}\| \leq N}$ column-wise and denote the vector by $\mathbf{w}^N(t)$, then

$$\frac{d\mathbf{w}^N}{dt} = A^N(t) \mathbf{w}^N + \mathbf{v}^N(t), \tag{2.6}$$

where A^N is a $(2N + 1)^2 \times (2N + 1)^2$ matrix and \mathbf{v}^N is a $(2N + 1)^2 \times 1$ vector determined by (2.5).

Define the Poincaré map $P : \mathbf{R}^{(2N+1)^2} \rightarrow \mathbf{R}^{(2N+1)^2}$ as:

$$P(\mathbf{x}) = \mathbf{X}(2\pi), \quad \mathbf{x} \in \mathbf{R}^{(2N+1)^2},$$

where $\mathbf{X}(t)$ solves

$$\begin{cases} \frac{d\mathbf{X}}{dt} = A^N(t) \mathbf{X} + \mathbf{v}^N(t), \\ \mathbf{X}(0) = \mathbf{x}. \end{cases} \tag{2.7}$$

Also define $P_0 : \mathbf{R}^{(2N+1)^2} \rightarrow \mathbf{R}^{(2N+1)^2}$,

$$P_0(\mathbf{x}) = \mathbf{X}_0(2\pi), \quad \mathbf{x} \in \mathbf{R}^{(2N+1)^2},$$

where $\mathbf{X}_0(t)$ solves

$$\begin{cases} \frac{d\mathbf{X}_0}{dt} = A^N(t) \mathbf{X}_0, \\ \mathbf{X}_0(0) = \mathbf{x}. \end{cases} \tag{2.8}$$

Let $\mathbf{e}_1, \mathbf{e}_2, \dots, \mathbf{e}_{(2N+1)^2}$ be the standard basis of $\mathbf{R}^{(2N+1)^2}$,

$$M = \begin{bmatrix} P_0(\mathbf{e}_1) & P_0(\mathbf{e}_2) & \cdots & P_0(\mathbf{e}_{(2N+1)^2}) \end{bmatrix}, \quad \mathbf{b} = P(\mathbf{0}),$$

then

$$P(\mathbf{x}) = M\mathbf{x} + \mathbf{b}, \quad \mathbf{x} \in \mathbf{R}^{(2N+1)^2}.$$

Let us impose

$$\int_{[0,2\pi]^2} w^N(\mathbf{x}, t) d\mathbf{x} = 0,$$

then $w_0^N(t) = 0$. Hence the initial value of $\mathbf{w}^N(t)$ is the solution to

$$\mathbf{x} = M\mathbf{x} + \mathbf{b}$$

with $\mathbf{x}_{2N^2+2N+1} = 0$.

2.4. Numerical method

We shall use $N_t + 1$ equally spaced grid points in the time interval $[0, 2\pi]$.

2.4.1. Assemble M and \mathbf{b} in the Poincaré map

Apply the classical Runge-Kutta method (e.g., RK4) to ODE (2.7) with zero initial value for N_t steps,

$$\begin{aligned} \hat{\mathbf{X}}_0 &= \mathbf{0}, \\ \hat{\mathbf{X}}_{n+1} &= \mathcal{L}(A^N, \mathbf{v}^N; \hat{\mathbf{X}}_n, t_n), \end{aligned}$$

where \mathcal{L} is the induction operator in RK4. Approximate \mathbf{b} by $\hat{\mathbf{b}} = \hat{\mathbf{X}}_{N_t+1}$. Similarly, apply RK4 to ODE (2.8) with initial value \mathbf{e}_j ,

$$\begin{aligned} \hat{\mathbf{X}}_{j,0} &= \mathbf{e}_j, \\ \hat{\mathbf{X}}_{j,n+1} &= \mathcal{L}(A^N, \mathbf{0}; \hat{\mathbf{X}}_{j,n}, t_n), \end{aligned}$$

for $j = 1, \dots, (2N + 1)^2$. Approximate $P_0(\mathbf{e}_j)$ by $\hat{\mathbf{m}}_j = \hat{\mathbf{X}}_{j,N_t+1}$ and M by

$$\hat{M} = \begin{bmatrix} \hat{\mathbf{m}}_1 & \hat{\mathbf{m}}_2 & \cdots & \hat{\mathbf{m}}_{(2N+1)^2} \end{bmatrix}.$$

In practice, only half of $\hat{\mathbf{m}}_j$'s are computed since $w_{-\mathbf{k}}^N = \overline{w_{\mathbf{k}}^N}$. It follows from (2.5) that $\hat{\mathbf{m}}_{2N^2+2N+1} = \mathbf{e}_{2N^2+2N+1}$. Let j_1, j_2, \dots, j_l be the vector indices corresponding to Fourier modes indices

$$\{\mathbf{k} = (k_1, k_2) \mid \mathbf{k} \neq \mathbf{0}, k_1 \leq k_2\},$$

where $l = 2N^2 + 2N$, and

$$\hat{\mathbb{X}}_0 = [\mathbf{e}_{j_1} \quad \mathbf{e}_{j_2} \quad \dots \quad \mathbf{e}_{j_l}],$$

then the following iteration for matrix

$$\hat{\mathbb{X}}_{n+1} = \mathcal{L}(A^N, \mathbf{0}; \hat{\mathbb{X}}_n, t_n)$$

gives

$$[\hat{\mathbf{m}}_{j_1} \quad \hat{\mathbf{m}}_{j_2} \quad \dots \quad \hat{\mathbf{m}}_{j_l}] = \hat{\mathbb{X}}_{N_t+1},$$

thus the matrix M in the Poincaré map is assembled. We note that the assembling of matrix M can be implemented in parallel.

2.4.2. Solve ODE (2.6) and estimate $D_{11,N}^E$

The initial data $\hat{\mathbf{x}}_0$ for discretized form of ODE (2.6) is solved from the linear system

$$\hat{\mathbf{x}}_0 = \hat{M}\hat{\mathbf{x}}_0 + \hat{\mathbf{b}}.$$

Again by RK4, the numerical periodic solution to ODE (2.6) is computed as

$$\begin{aligned} \hat{\mathbf{w}}_0^N &= \hat{\mathbf{x}}_0, \\ \hat{\mathbf{w}}_{n+1}^N &= \mathcal{L}(A^N, \mathbf{v}^N; \hat{\mathbf{w}}_n^N, t_n). \end{aligned}$$

For $n = 0, 1, \dots, N_t$, reorder $\hat{\mathbf{w}}_n^N$ as Fourier modes $\{\hat{w}_{\mathbf{k},n}^N\}_{\|\mathbf{k}\| \leq N}$, then $D_{11,N}^E$ is estimated by

$$\hat{D}_{11,N}^E = D_0 \left(1 + \frac{1}{N_t} \sum_{n=1}^{N_t} \sum_{\|\mathbf{k}\| \leq N} |\mathbf{k}|^2 |\hat{w}_{\mathbf{k},n}^N|^2 \right).$$

2.5. Numerical results

In this section, we first present computational results of D_{11}^E by spectral method and Poincaré map for small D_0 , recovering the early finding in [2] on time periodic cellular flows. We then perform a parameter dependence study of D_{11}^E on a family of such flows, and discover a non-monotone relationship between D_{11}^E and the amount of chaos in the flows. Similar results hold for D_{12}^E .

2.5.1. Two-dimensional time-dependent flow

As in [2], we consider the time periodic cellular flow with chaotic Lagrangian trajectories:

$$v(\mathbf{x}, t) = \cos(x_2) + \sin(x_2) \cos(t), \tag{2.9a}$$

$$\tilde{v}(\mathbf{x}, t) = \cos(x_1) + \sin(x_1) \cos(t). \tag{2.9b}$$

Rewrite

$$v(\mathbf{x}, t) = \frac{1}{2}(1 - i \cos t) e^{ix_2} + \frac{1}{2}(1 + i \cos t) e^{-ix_2},$$

$$\tilde{v}(\mathbf{x}, t) = \frac{1}{2}(1 - i \cos t) e^{ix_1} + \frac{1}{2}(1 + i \cos t) e^{-ix_1}.$$

Set $\mathbf{e}_1 = (1, 0)$, $\mathbf{e}_2 = (0, 1)$, then

$$v_{\pm \mathbf{e}_2}(t) = \tilde{v}_{\pm \mathbf{e}_1}(t) = \frac{1}{2}(1 \mp i \cos t),$$

$$v_{\mathbf{k}}(t) = 0, \quad \mathbf{k} \neq \pm \mathbf{e}_2,$$

$$\tilde{v}_{\mathbf{k}}(t) = 0, \quad \mathbf{k} \neq \pm \mathbf{e}_1.$$

Hence (2.5) is reduced to

$$\begin{aligned} \frac{dw_{\mathbf{k}}^N}{dt} + D_0 |\mathbf{k}|^2 w_{\mathbf{k}}^N + \frac{1}{2} [k_1 (i + \cos t) w_{\mathbf{k}-\mathbf{e}_2}^N + k_1 (i - \cos t) w_{\mathbf{k}+\mathbf{e}_2}^N \\ + k_2 (i + \cos t) w_{\mathbf{k}-\mathbf{e}_1}^N + k_2 (i - \cos t) w_{\mathbf{k}+\mathbf{e}_1}^N] + v_{\mathbf{k}} = 0. \end{aligned}$$

Both A^N and \mathbf{v}^N are sparse. Estimates of $D_{11,N}^E$ for some varied $D_0/N/N_t$'s are shown in Tables 1-5. $D_{11,N}^E$'s vs. D_0 are plotted in Fig. 1 which resembles Fig. 4 of [2] in the regime $D_0 \leq 0.1$.

Table 1: $\hat{D}_{11,N}^E$ for flow (2.9) with $D_0 = 10^{-2}$.

$\hat{D}_{11,N}^E \backslash N$					
$N_t \backslash$	30	35	40	45	50
1000	1.3412	1.3412	1.3412	1.3412	1.3412
1500	1.3412	1.3412	1.3412	1.3412	1.3412

Table 2: $\hat{D}_{11,N}^E$ for flow (2.9) with $D_0 = 10^{-3}$.

$\hat{D}_{11,N}^E \backslash N$					
$N_t \backslash$	40	45	50	55	60
1000	1.3847	1.3787	1.3790	1.3795	1.3778
1500	1.3790	1.3795	1.3778	1.3773	1.3772

Table 3: $\hat{D}_{11,N}^E$ for flow (2.9) with $D_0 = 10^{-4}$.

$\hat{D}_{11,N}^E \backslash N_t$	N	40	45	50	55	60
1000		1.5448	1.5961	1.5087	1.5035	1.4936
1500		1.5459	1.5971	1.5099	1.5050	1.4949
2000		1.5460	1.5972	1.5101	1.5051	1.4951

Table 4: $\hat{D}_{11,N}^E$ for flow (2.9) with $D_0 = 10^{-5}$.

$\hat{D}_{11,N}^E \backslash N_t$	N	55	60	65	70	75	80
2000		1.6774	1.6268	1.7604	1.7528	1.8265	1.6984
2500		1.6793	1.6301	1.7651	1.7558	1.8336	1.7056

Table 5: $\hat{D}_{11,N}^E$ for flow (2.9) with $D_0 = 10^{-6}$.

$\hat{D}_{11,N}^E \backslash N_t$	N	55	60	65	70	75	80
2000		1.5676	1.6114	1.7351	1.7074	2.0494	1.5528
2500		1.6270	1.7410	1.8016	1.7882	2.1849	1.6831

2.5.2. Two-dimensional time-dependent flow with $\theta \in (0, 1]$

Let us consider now the one parameter family of time periodic cellular flows

$$v(\mathbf{x}, t) = \cos(x_2) + \theta \sin(x_2) \cos(t), \tag{2.10a}$$

$$\tilde{v}(\mathbf{x}, t) = \cos(x_1) + \theta \sin(x_1) \cos(t). \tag{2.10b}$$

As θ increases, the flow trajectories are more and more mixing and chaotic [17]. The Fourier modes for the flow are:

$$v_{\pm e_2}(t) = \tilde{v}_{\pm e_1}(t) = \frac{1}{2} (1 \mp i\theta \cos t),$$

$$v_{\mathbf{k}}(t) = 0, \quad \mathbf{k} \neq \pm e_2,$$

$$\tilde{v}_{\mathbf{k}}(t) = 0, \quad \mathbf{k} \neq \pm e_1.$$

Similarly, (2.5) is reduced to

$$\frac{dw_{\mathbf{k}}^N}{dt} + D_0 |\mathbf{k}|^2 w_{\mathbf{k}}^N + \frac{1}{2} [k_1 (i + \theta \cos t) w_{\mathbf{k}-e_2}^N + k_1 (i - \theta \cos t) w_{\mathbf{k}+e_2}^N + k_2 (i + \theta \cos t) w_{\mathbf{k}-e_1}^N + k_2 (i - \theta \cos t) w_{\mathbf{k}+e_1}^N] + v_{\mathbf{k}} = 0.$$

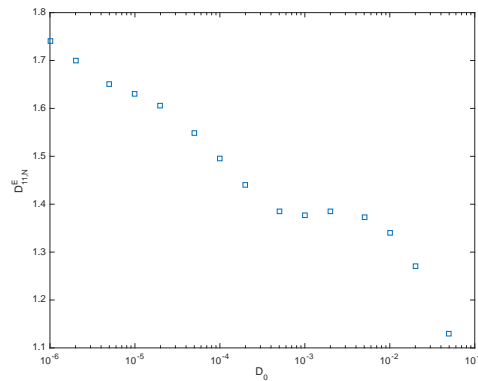


Figure 1: Computed $D_{11,N}^E$ vs. D_0 for flow (2.9), resembling Fig. 4 of [2] in the regime $D_0 \leq 0.1$.

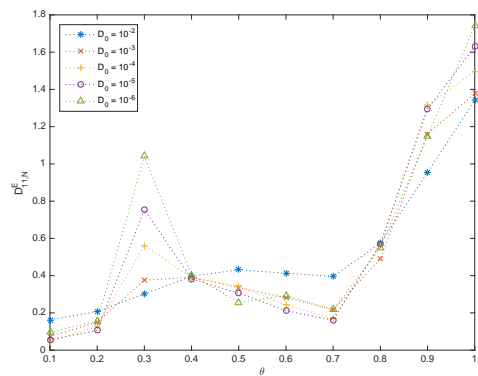


Figure 2: $D_{11,N}^E$ vs. θ for the time periodic cellular flow (2.10) with numerical parameters in Table 7.

A^N and \mathbf{v}^N are still sparse. Estimates $\hat{D}_{11,N}^E$ are shown in Table 6 and plotted in Fig. 2. These results are computed according to numerical parameters in Table 7. Larger values of N/N_t did not alter the results significantly. We observed a non-monotone dependence of D_{11}^E vs. θ in the small D_0 regime, though the overall trend is that D_{11}^E increases with the amount of chaos in the flows.

2.5.3. Estimates of D_{12}^E

The second component of $\mathbf{w} = (w, \tilde{w})$ can be approximated by Fourier modes in a similar way to (2.4),

$$\tilde{w}^N(\mathbf{x}, t) = \sum_{\|\mathbf{k}\| \leq N} \tilde{w}_{\mathbf{k}}^N(t) e^{i\mathbf{k} \cdot \mathbf{x}}.$$

Table 6: Computed $D_{11,N}^E$ vs. θ for the time periodic cellular flow (2.10).

$\hat{D}_{11,N}^E \backslash D_0$	10^{-2}	10^{-3}	10^{-4}	10^{-5}	10^{-6}
θ					
0.1	0.1625	0.0733	0.0466	0.0560	0.0954
0.2	0.2079	0.1507	0.1270	0.1054	0.1573
0.3	0.3020	0.3754	0.5615	0.7544	1.0406
0.4	0.3967	0.3921	0.3887	0.3820	0.4040
0.5	0.4315	0.3348	0.3432	0.3063	0.2563
0.6	0.4129	0.2823	0.2425	0.2120	0.2934
0.7	0.3954	0.2177	0.1708	0.1612	0.2156
0.8	0.5740	0.4902	0.5625	0.5708	0.5497
0.9	0.9543	1.1608	1.3140	1.2939	1.1494
1.0	1.3412	1.3778	1.4951	1.6301	1.7410

Table 7: Numerical parameters for computing $\hat{D}_{11,N}^E$.

D_0	10^{-2}	10^{-3}	10^{-4}	10^{-5}	10^{-6}
N	50	60	60	60	60
N_t	1500	1500	2000	2500	2500

Hence an estimate of D_{12}^E is

$$D_{12,N}^E = D_0 \sum_{\|\mathbf{k}\| \leq N} |\mathbf{k}|^2 \langle w_{\mathbf{k}}^N \overline{w_{\mathbf{k}}^N} \rangle.$$

Computed $D_{12,N}^E$ vs. D_0 for flow (2.9) are plotted in Fig. 3. $D_{12,N}^E$'s vs. θ for flow (2.10) with the same numerical parameters in Table 7 are plotted in Fig. 4.

3. Orthogonal adaptive basis learning

In this section, we discuss orthogonal adaptive basis construction via a learning process based on the spectral solutions.

3.1. Snapshots of periodic solutions and SVD

Let $\{\hat{\mathbf{w}}_n^{*N}\}_{n=0}^{N_t}$ be a numerical periodic solution to (2.5) for some D_0^* , form the matrix

$$W = [\hat{\mathbf{w}}_0^{*N} \quad \hat{\mathbf{w}}_1^{*N} \quad \dots \quad \hat{\mathbf{w}}_{N_t}^{*N}],$$

and apply singular value decomposition to W ,

$$W = U\Sigma V.$$

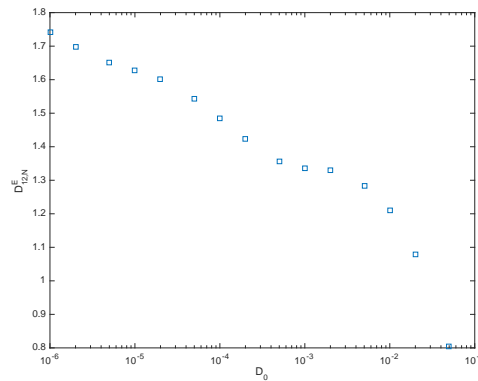


Figure 3: Computed $D_{12,N}^E$ vs. D_0 for flow (2.9).

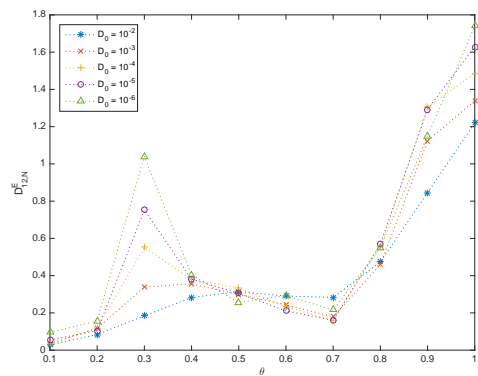


Figure 4: $D_{12,N}^E$ vs. θ for the time periodic cellular flow (2.10) with numerical parameters in Table 7.

Consider SVD of numerical solutions for the time periodic cellular flow (2.9)

$$v(\mathbf{x}, t) = \cos(x_2) + \sin(x_2) \cos(t),$$

$$\tilde{v}(\mathbf{x}, t) = \cos(x_1) + \sin(x_1) \cos(t).$$

Snapshots of numerical solutions to (2.3) at $D_0^* = 10^{-3}, 10^{-4}$ are shown in Figs. 5-6 where we see thinner layered structures arise as D_0 becomes smaller. Singular values of W for several D_0 's are plotted in Fig. 7 which shows rapid decay beyond 250 out of 3000 modes, uniformly as $D_0 \downarrow 0$.

3.2. ODEs from adaptive basis and poincaré map

Denote by \mathbf{u}_j the j th column of U . For $m > 0$, the adaptive orthogonal basis consists of the columns of the matrix:

$$U_m = [\mathbf{u}_1 \quad \mathbf{u}_2 \quad \cdots \quad \mathbf{u}_m].$$

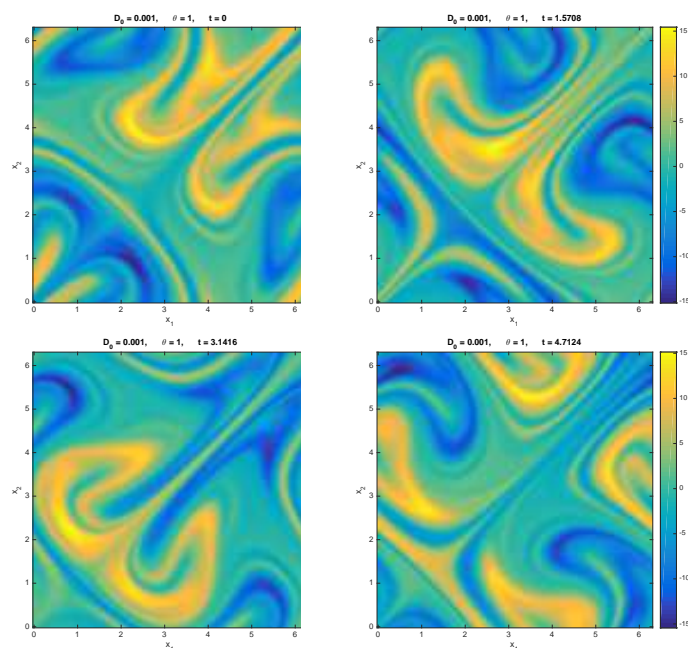


Figure 5: Sampled snapshots of solution to (2.3) with $D_0^* = 10^{-3}$, appearance of layered structures.

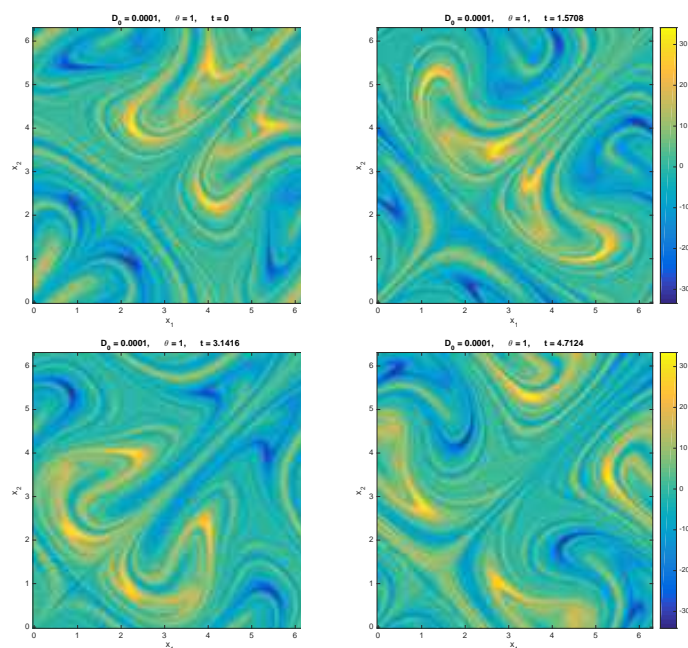


Figure 6: Sampled snapshots of solution to (2.3) with $D_0^* = 10^{-4}$, formation of thin layers.

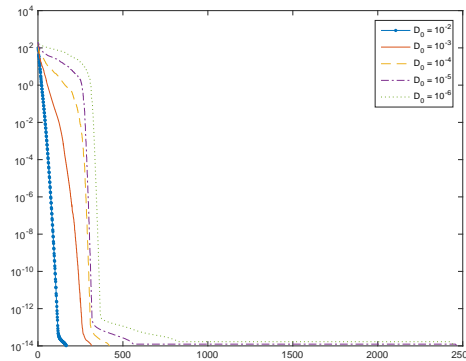


Figure 7: Singular values of numerical periodic solution matrices, rapid decay uniformly in $D_0 \downarrow 0$.

Figs. 8-9 are visualizations of $\mathbf{u}_1, \mathbf{u}_2, \mathbf{u}_5, \mathbf{u}_6$ for the flow (2.9).

Given $D_0 > 0$, let us write the solution to (2.6) in the orthogonal adaptive basis as:

$$\mathbf{w}^N(t) = U_m \mathbf{a}^N(t),$$

where $\mathbf{a}(t) = [a_1(t), a_2(t), \dots, a_m(t)]^T$ is periodic, then

$$\frac{d\mathbf{a}^N}{dt} = \bar{U}_m^T A^N(t) U_m \mathbf{a}^N + \bar{U}_m^T \mathbf{v}^N(t). \tag{3.1}$$

Hence an approximation of solution to (2.6) can be obtained by solving (3.1).

Similar to the approach used for the Fourier modes, let us define the Poincaré map associated to the ODE (3.1)

$$P^a(\mathbf{x}) = M^a \mathbf{x} + \mathbf{b}^a, \quad \mathbf{x} \in \mathbf{R}^m,$$

where M^a is an $m \times m$ matrix and \mathbf{b}^a is an $m \times 1$ vector.

- \mathbf{b}^a can be solved numerically by

$$\begin{aligned} \hat{\mathbf{X}}_0 &= \mathbf{0}, \\ \hat{\mathbf{X}}_{n+1} &= \mathcal{L} \left(\bar{U}_m^T A^N U_m, \bar{U}_m^T \mathbf{v}^N; \hat{\mathbf{X}}_n, t_n \right), \end{aligned}$$

and $\hat{\mathbf{b}} = \hat{\mathbf{X}}_{N_t+1}$. For $j = 1, \dots, m$, the j th column of the numerical approximation \hat{M}^a for M^a is computed by $\hat{\mathbf{m}}_j^a = \hat{\mathbf{X}}_{j, N_t+1}$ through iteration

$$\begin{aligned} \hat{\mathbf{X}}_{j,0} &= \mathbf{e}_j, \\ \hat{\mathbf{X}}_{j,n+1} &= \mathcal{L} \left(\bar{U}_m^T A^N U_m, \mathbf{0}; \hat{\mathbf{X}}_{j,n}, t_n \right), \end{aligned}$$

where $\mathbf{e}_1, \dots, \mathbf{e}_m$ are standard basis of \mathbf{R}^m .

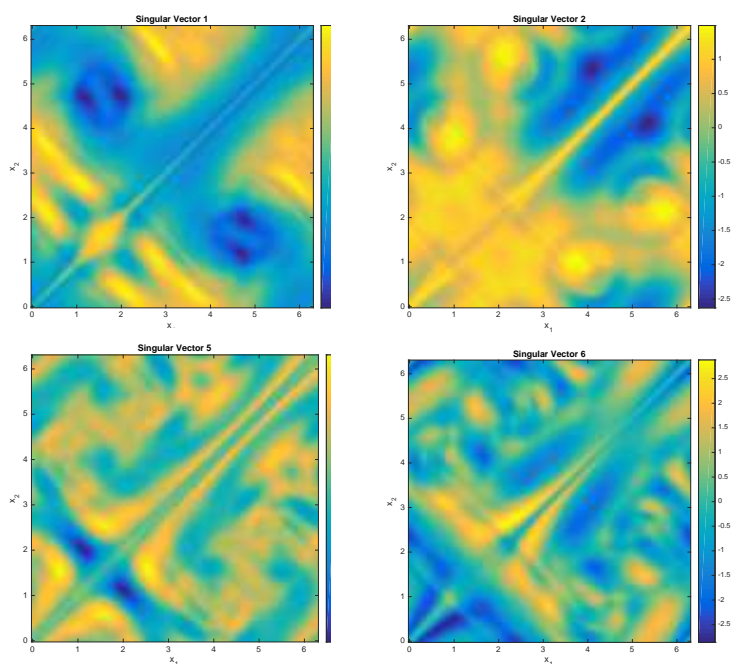


Figure 8: Sampled singular vectors with $D_0^* = 10^{-3}$, $N = 60$, $N_t = 1500$.

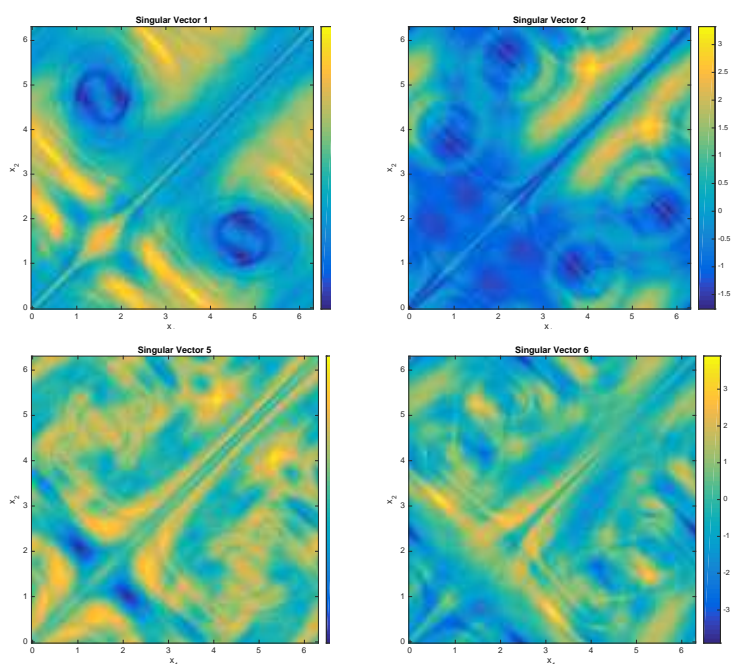


Figure 9: Sampled singular vectors with $D_0^* = 10^{-4}$, $N = 60$, $N_t = 2000$.

- The numerical periodic solution to ODE (3.1) is computed as

$$\begin{aligned} \hat{\mathbf{a}}_0^N &= \hat{\mathbf{x}}_0, \\ \hat{\mathbf{a}}_{n+1}^N &= \mathcal{L}(\bar{U}_m^T A^N U_m, \bar{U}_m^T \mathbf{v}^N; \hat{\mathbf{a}}_n^N, t_n), \end{aligned}$$

where $\hat{\mathbf{x}}_0$ solves

$$\hat{\mathbf{x}}_0 = \hat{M}^a \hat{\mathbf{x}}_0 + \hat{\mathbf{b}}^a.$$

- Reorder

$$\hat{\mathbf{w}}_n^N = U_m \hat{\mathbf{a}}_n^N$$

as Fourier modes $\{\hat{w}_{\mathbf{k},n}^N\}_{\|\mathbf{k}\|\leq N}$, $n = 0, 1, \dots, N_t$. $D_{11,N}^E$ is estimated by

$$\hat{D}_{11,N}^{E,a} = D_0 \left(1 + \frac{1}{N_t} \sum_{n=1}^{N_t} \sum_{\|\mathbf{k}\|\leq N} |\mathbf{k}|^2 |\hat{w}_{\mathbf{k},n}^N|^2 \right).$$

3.3. Numerical results of orthogonal adaptive basis

We show computational results on residual diffusion from the orthogonal adaptive basis on time periodic cellular flows. The main goal is to maintain enough accuracy at low costs.

3.3.1. Two-dimensional time-dependent flow (2.9)

- $D_0^* = 10^{-3}$, $N = 60$, $N_t = 1500$ with $m = 100$ (the number of adaptive basis functions).

In Table 8, $D_{11,N}^E$ from the Fourier basis (with $N_t = 2000$) for flow (2.9) at varied D_0 's are shown along with those from the orthogonal adaptive basis, denoted by $\hat{D}_{11,N}^{E,a}$. To measure the reduction in the number of basis functions, we define $r = m / (2N + 1)^2$ as the ratio of the number of adaptive basis functions and that of the Fourier basis functions. The estimates by adaptive basis are close to those from the Fourier basis when D_0 is not far from $D_0^* = 10^{-3}$ (the D_0 value where the adaptive basis is constructed or trained). The robustness of adaptive basis hinges on how fast the error grows as the testing occurs at a D_0 value deviating from the training value D_0^* .

The energy of a truncated Fourier expansion is:

$$\mathcal{E} \left(\sum_{\|\mathbf{k}\|\leq N} z_{\mathbf{k}}^N(t) e^{i\mathbf{k}\cdot\mathbf{x}} \right) = D_0 \sum_{\|\mathbf{k}\|\leq N} |\mathbf{k}|^2 \langle z_{\mathbf{k}}^N \bar{z}_{\mathbf{k}}^N \rangle.$$

Table 8: $\hat{D}_{11,N}^{E,a}$ and $\hat{D}_{11,N}^E$ for flow (2.9) with $D_0^* = 10^{-3}$, $r = 0.68\%$.

D_0	10^{-3}	9×10^{-4}	8×10^{-4}	7×10^{-4}	6×10^{-4}
$\hat{D}_{11,N}^{E,a}$	1.3772	1.4050	1.4337	1.4632	1.4931
$\hat{D}_{11,N}^E$	1.3772	1.3765	1.3763	1.3772	1.3796
relative error	0	2.1%	4.2%	6.3%	8.2%
D_0	5×10^{-4}	4×10^{-4}	3×10^{-4}	2×10^{-4}	10^{-4}
$\hat{D}_{11,N}^{E,a}$	1.5229	1.5515	1.5775	1.6047	1.7191
$\hat{D}_{11,N}^E$	1.3847	1.3940	1.4105	1.4395	1.4951
relative error	10.0%	11.3%	11.8%	11.5%	15.0%

Table 9: $\hat{D}_{11,N}^{E,a}$ and $\hat{D}_{11,N}^E$ for flow (2.9) with $D_0^* = 10^{-4}$, $r = 1.37\%$.

D_0	10^{-4}	9×10^{-5}	8×10^{-5}	7×10^{-5}	6×10^{-5}
$\hat{D}_{11,N}^{E,a}$	1.4951	1.5042	1.5129	1.5208	1.5272
$\hat{D}_{11,N}^E$	1.4951	1.5036	1.5131	1.5236	1.5355
relative error	0	0	0	0.2%	0.5%
D_0	5×10^{-5}	4×10^{-5}	3×10^{-5}	2×10^{-5}	10^{-5}
$\hat{D}_{11,N}^{E,a}$	1.5314	1.5313	1.5242	1.5107	1.5243
$\hat{D}_{11,N}^E$	1.5492	1.5649	1.5834	1.6052	1.6301
relative error	1.1%	2.1%	3.7%	5.9%	6.5%

Let $\{\hat{z}_{\mathbf{k},n}^N\}_{n=1}^{N_t+1}$ be the numerical approximation of $z_{\mathbf{k}}^N(t)$, then the energy for $\sum_{\|\mathbf{k}\| \leq N} z_{\mathbf{k}}^N(t) \cdot e^{i\mathbf{k} \cdot \mathbf{x}}$ can be approximated by

$$\mathcal{E} \left(\sum_{\|\mathbf{k}\| \leq N} z_{\mathbf{k}}^N(t) e^{i\mathbf{k} \cdot \mathbf{x}} \right) \approx \frac{D_0}{N_t} \sum_{n=1}^{N_t} \sum_{\|\mathbf{k}\| \leq N} |\mathbf{k}|^2 |\hat{z}_{\mathbf{k},n}^N|^2.$$

Figs. 10-11 show the energy vs. the number of modes in the solutions solved by Fourier basis and the learned orthogonal adaptive basis. Clearly, a much smaller number of basis functions is needed to represent the same level of energy by the adaptive basis than by the Fourier basis.

- $D_0^* = 10^{-4}$, $N = 60$, $N_t = 2000$ with $m = 200$

Computations of $D_{11,N}^E$ and $\hat{D}_{11,N}^{E,a}$ for the flow (2.9) at smaller D_0 's are shown in Table 9. The comparisons of energy growth vs. the number of basis functions are shown in Figs. 12-13. Here $N_t = 2500$ in computation of $\hat{D}_{11,N}^E$ with the Fourier basis. Interestingly, the relative errors of solutions via the orthogonal adaptive basis drop considerably at smaller D_0 , suggesting that the basis learning is effective for computing residual diffusion.

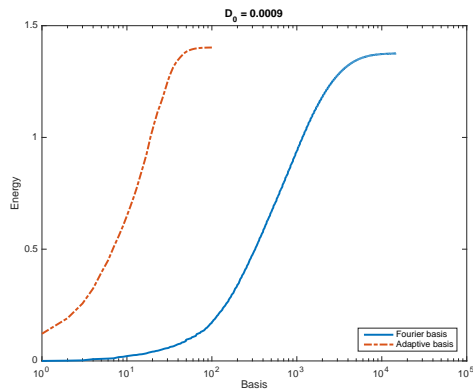


Figure 10: Energy growth vs. the number of adaptive (dashdot, red) and Fourier (solid, blue) basis functions for $D_0 = 9 \times 10^{-4}$.

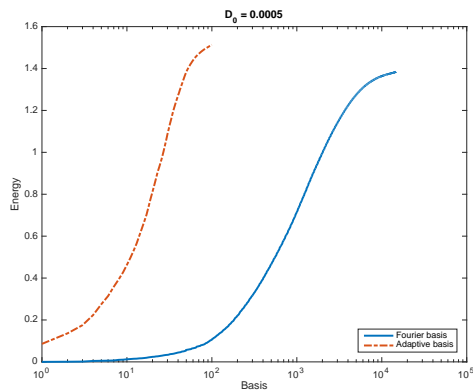


Figure 11: Energy growth vs. the number of adaptive (dashdot, red) and Fourier (solid, blue) basis functions for $D_0 = 5 \times 10^{-4}$.

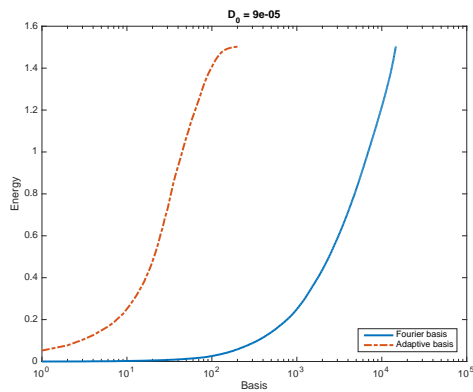


Figure 12: Energy growth vs. the number of adaptive (dashdot, red) and Fourier (solid, blue) basis functions for $D_0 = 9 \times 10^{-5}$.

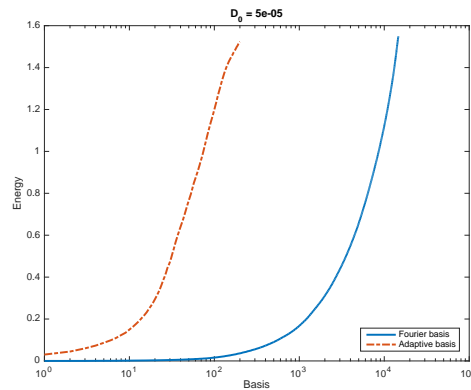


Figure 13: Energy growth vs. the number of adaptive (dashdot, red) and Fourier (solid, blue) basis functions for $D_0 = 5 \times 10^{-5}$.

3.3.2. Two-dimensional time-dependent flow (2.10) with $\theta \in (0, 1]$

Adaptive orthogonal basis can also be trained from a periodic solution at a θ value and applied to another flow at a nearby θ value. For instance, assemble W in Section 3.1 with snapshots of a periodic solution for some D_0^* and flow (2.10) with parameter θ^* . Periodic solutions as well as effective diffusivities at the same D_0^* but different θ 's can be approximated as in Section 3.2. However, the dependence of D_{11}^E on θ seems very sensitive especially at small D_0 , as the test results indicate below.

- $\theta^* = 0.7, D_0 = 10^{-3}, 10^{-4}$ with $m = 100$
 Estimates of $D_{11,N}^E$ for flow (2.10) with $D_0 = 10^{-3}, 10^{-4}$ and varied θ 's by reduced basis trained with $\theta^* = 0.7$, denoted by $\hat{D}_{11,N}^{E,a}$, as well as results from Fourier basis, are presented in Tables 10-11.
- $\theta^* = 0.4, D_0 = 10^{-3}, 10^{-4}$ with $m = 100$

Table 10: $\hat{D}_{11,N}^{E,a}$ and $\hat{D}_{11,N}^E$ for flow (2.10) with $D_0 = 10^{-3}$ and $\theta^* = 0.7, N = 60, N_t = 1500, r = 0.68\%$.

θ	0.7	0.71	0.72	0.73	0.74	0.75
$\hat{D}_{11,N}^{E,a}$	0.2177	0.2138	0.2101	0.2065	0.2029	0.1993
$\hat{D}_{11,N}^E$	0.2177	0.2251	0.2368	0.2509	0.2715	0.2978
relative error	0	5.0%	10.9%	17.7%	25.3%	33.1%

Table 11: $\hat{D}_{11,N}^{E,a}$ and $\hat{D}_{11,N}^E$ for flow (2.10) with $D_0 = 10^{-4}$ and $\theta^* = 0.7, N = 60, N_t = 2000, r = 0.68\%$.

θ	0.7	0.71	0.72	0.73	0.74	0.75
$\hat{D}_{11,N}^{E,a}$	0.1725	0.1636	0.1571	0.1536	0.1518	0.1491
$\hat{D}_{11,N}^E$	0.1708	0.1838	0.1957	0.2063	0.2360	0.2849
relative error	1.0%	10.1%	19.7%	25.5%	35.7%	47.7%

Table 12: $\hat{D}_{11,N}^{E,a}$ and $\hat{D}_{11,N}^E$ for flow (2.10) with $D_0 = 10^{-3}$ and $\theta^* = 0.4$, $N = 60$, $N_t = 1500$, $r = 0.68\%$.

θ	0.4	0.41	0.42	0.43	0.44	0.45
$\hat{D}_{11,N}^{E,a}$	0.3921	0.3700	0.3523	0.3380	0.3261	0.3161
$\hat{D}_{11,N}^E$	0.3921	0.3772	0.3637	0.3528	0.3451	0.3405
relative error	0	2.0%	3.1%	4.2%	5.5%	7.2%

Table 13: $\hat{D}_{11,N}^{E,a}$ and $\hat{D}_{11,N}^E$ for flow (2.10) with $D_0 = 10^{-4}$ and $\theta^* = 0.4$, $N = 60$, $N_t = 2000$, $r = 0.68\%$.

θ	0.4	0.41	0.42	0.43	0.44	0.45
$\hat{D}_{11,N}^{E,a}$	0.3888	0.3795	0.3788	0.3810	0.3823	0.3792
$\hat{D}_{11,N}^E$	0.3887	0.3516	0.3187	0.3027	0.3041	0.3195
relative error	0	8.0%	18.9%	25.9%	25.7%	18.7%

Estimates of $D_{11,N}^E$ for flow (2.10) with $D_0 = 10^{-3}, 10^{-4}$ and varied θ 's by reduced basis trained with $\theta^* = 0.4$ as well as results from Fourier basis are shown in Tables 12-13.

4. Concluding remarks

We constructed orthogonal adaptive basis functions based on learning from the fully resolved spectral method at sampled small molecular diffusivities to aid the low cost computation of residual diffusivities. Even though solutions develop large gradients and demand a large number of Fourier modes to resolve, the adaptive basis functions maintain accuracy of residual diffusivities at much smaller number of basis functions, uniform in the limit of zero molecular diffusivity. A line of future work is to increase the generalization and robustness of the adaptive basis functions by learning through robust versions of singular value decomposition techniques such as robust principal component analysis.

Acknowledgments JX was partially supported by NSF grant DMS-1211179. YY was partially supported by DMS-0901460 and NSF CAREER award DMS-1151919. JL was partially supported by DMS-1151919, and DMS-1211179. We thank Prof. Russel Caflisch for helpful conversations and his interest during the preparation of the work.

References

- [1] A. BENSOUSSAN, J. L. LIONS, AND G. PAPANICOLAOU, *Asymptotic Analysis for Periodic Structures*, AMS Chelsea Publishing, 2011.
- [2] L. BIFERALE, A. CRISTINI, M. VERGASSOLA AND A. VULPIANI, *Eddy diffusivities in scalar transport*, *Phys. Fluids*, 7(11) (1995), pp. 2725–2734.
- [3] R. CAMASSA AND S. WIGGINS, *Chaotic advection in a Rayleigh-Bénard flow*, *Phys. Rev. A*, 43(2) (1990), pp. 774–797.

- [4] S. CHILDRESS AND A. GILBERT, *Stretch, Twist, Fold: The Fast Dynamo*, Lecture Notes in Physics Monographs, No. 37, 1995, Springer.
- [5] A. FANNJIANG AND G. PAPANICOLAOU, *Convection enhanced diffusion for periodic flows*, SIAM J. Appl. Math., 54(2) (1994), pp. 333–408.
- [6] S. HEINZE, *Diffusion-advection in cellular flows with large Peclet numbers*, Archive Rational Mech. Anal., 168(4) (2003), pp. 329–342.
- [7] P. HOLMES, J. LUMLEY AND G. BERKOOZ, *Turbulence, coherent structures, dynamical systems and symmetry*, AIAA J., 36(3) (1998), pp. 496–496.
- [8] J. LUMLEY, *Coherent structures in turbulence*, Transition and Turbulence, (1981), pp. 215–241.
- [9] A. MAJDA AND P. KRAMER, *Simplified models for turbulent diffusion: theory, numerical modelling, and physical phenomena*, Phys. Reports, 314 (1999), pp. 237–574.
- [10] B. MURPHY, E. CHERKAEV, J. XIN, J. ZHU AND K. GOLDEN, *Spectral analysis and computation of effective diffusivity in space-time periodic incompressible flows*, Ann. Math. Sci. Appl., 2(1) (2017), pp. 3–66, CAM Report, pp. 15–63, UCLA, 2016.
- [11] A. NOVIKOV AND L. RYZHIK, *Boundary layers and KPP fronts in a cellular flow*, Arch. Rational Mech. Anal. 184(1) (2007), pp. 23–48.
- [12] A. QUARTERONI AND G. ROZZA, *Reduced Order Methods for Modeling and Computational Reduction*, MS&A, Vol. 9, Springer, 2014.
- [13] G. TAYLOR, *Diffusion by continuous movements*, Proc. London Math. Soc., 20 (1922).
- [14] J. XIN AND Y. YU, *Sharp asymptotic growth laws of turbulent flame speeds in cellular flows by inviscid Hamilton-Jacobi models*, Annales l'Institut H. Poincaré Analyse Non Linéaire, 30(6) (2013), pp. 1049–1068.
- [15] J. XIN AND Y. YU, *Front quenching in G-equation model induced by straining of cellular flow*, Arch. Rational Mech. Anal., 214 (2014), pp. 1–34.
- [16] A. ZLATOŠ, *Sharp asymptotics for KPP pulsating front speed-up and diffusion enhancement by flows*, Arch. Ration. Mech. Anal., 195 (2010), pp. 441–453.
- [17] P. ZU, L. CHEN AND J. XIN, *A computational study of residual KPP front speeds in time-periodic cellular flows in the small diffusion limit*, Phys. D, 311–312 (2015), pp. 37–44.